Micromechanics of sea ice frictional slip from test basin scale experiments

Peter R. Sammonds[1], Daniel C. Hatton[1,2] and Daniel L. Feltham[3]

*[1]Rock and Ice Physics Laboratory, Department of Earth Sciences, University College London, Gower Street, London, UK WC1E 6BT (*p.sammonds@ucl.ac.uk). [2]School of Marine Science and Engineering, Plymouth University, Drake Circus, Plymouth, UK PL4 8AA. [3]Centre for Polar Observation and Modelling, Department of Meteorology, University of Reading, PO Box 243, Reading, UK RG6 6BB*

*Author for correspondence (p.sammonds@ucl.ac.uk)

Keywords: sea ice friction; micromechanics; scaling

July 10, 2016

Summary

1. Introduction

Understanding ice friction is important across many scales. At the micro-scale, fundamental physical processes of asperity contact affect icing on structures and friction in winter sports (e.g., Seymour-Pierce et al., this volume) [1]; at intermediate scales in arctic engineering ice friction determines the resistance to ship movement (e.g., Scourfield et al. 2015) [2], or in glaciology, ice stream dynamics (e.g., McCarthy et al., this volume) [3]; at the Arctic Basin scale, ice friction is a control on the distribution and thickness of sea ice (e.g., Weiss and Dansereau, this volume [4]); on a planetary scale, friction has a role in planetary dynamics (e.g., Middleton et al, this volume [5]). However, ice friction is also a controversial topic involving complex processes such as fracture, creep, pressure melting, pre-melting and frictional heating (e.g., Hatton et al., 2009) [6]. In this paper we address the micromechanics of sea ice friction, derived from intermediate scale experiments, in order that they might be upscaled to the Arctic Basin scale.

Sea ice is notably brittle (e.g., Sammonds et al., 1998) [7]. In the Arctic Ocean, ice deformation causes formation of thin ice through creation of open-water leads and thick ice through ice rafting and ridging. RADARSAT imagery shows that the principal observation of the arctic sea ice cover during winter are the presence of long lineaments, some of which extend across large parts of the Arctic Basin and show high shear deformation (Kwok, 2001) [8]. Marko and Thomson (1997) [9] suggested that these lineaments are analogous to strike-slip faults in the Earth's crust. Friction plays a key role in ice rafting and ridging (Hopkins et al., 1999) [10]. Stick-slip friction has been observed in laboratory experiments on multi-year sea ice (Sammonds et al., 1998) [7] and one can imagine it playing a key role in sea ice dynamics and explain behaviour observed in ice tank experiments (Tukkuri and Lensu, 2002) [11]. So it is clear that a realistic sea ice rheology has to incorporate brittle-discontinuous slip displacement on these faults (Sammonds and Rist, 2001) [12]. While Taylor et al. (2006) [13] have proposed a homogenization methodology to determine a continuum-scale sea ice rheology from consideration of ice interactions within a representative region to enable the upscaling.

Experimental work on the mechanics of ice friction has shown that at high enough sliding speeds, the low friction of ice is caused by a lubricating layer of melt water generated by frictional heating

(Bowden and Tabor, 1964) [14]. The water-lubrication mechanism has been investigated by Evans et al. (1976) [15] in the laboratory using a slider block and modelled by Oksanen and Keinonen (1982) [16] and Nielsen et al. (2008) [17]. Persson (2015) [18] proposed that softening results in a thin layer of disordered ice, with a shear strength which decreases continuously as the ice surface temperature approaches the bulk melting temperature at intermediate speeds. At low sliding speeds, where frictional heating does not play a role, the coefficient of friction of ice can be considerably higher. Rist (1997) [19] attributes this to elastically deforming asperities undergoing shear fracture. Plastic creep deformation and adhesion have also been proposed as the cause of higher friction (Barnes et al., 1971 [20]; Kennedy et al, 2000 [21]: Maeno et al. 2003 [22]; Schulson and Fortt, 2012 [23]). Hatton et al. (2009) [6] constructed a theoretical procedure for predicting which mechanisms of normal deformation (ductile or elastic) and shear failure (ductile, brittle, or melting and hydrodynamic lubrication) will apply under particular circumstances, thus unifying the various micro-mechanical perspectives.

Ice friction is usually modelled by Amonton's classical friction law, $\tau = \mu\sigma$, where τ is the shear stress, μ is the coefficient of friction, and σ is the normal stress (e.g., Bowden and Tabor, 1964 [14]). or by Coulomb's law which introduces a cohesive term (e.g., Schulson and Fortt, 2011 [23]). Rist's (1997 [19]) re-analysis of ice friction data where surface melting is unlikely to occur, showed that ice follows a well-defined non-linear friction law in which $\tau \propto \sigma^{2/3}$, in accordance with Archard's (1957) [24] law. Lishman et al. (2011) [25] introduced a rate and state friction law which combined the classical frictional law with phenomenological curves for the dependence of shear stress on sliding velocity and on the time for which the ice has been stationary. But in rock and earthquake mechanics (Ohnaka and feng-Shen, 1999) [26], it has been recognised that the frictional slip displacement is an important parameter. This has received little attention in ice mechanics and we would argue that this, or a slip time (Lishman et al., 2013) [27] needs to be included explicitly in rheological models of arctic sea ice.

In order to build a micro mechanical friction model that can be upscaled we have conducted intermediate scale experiments in an environmental test basin, usually employed for testing model ships, where large floating saline ice floes are pushed past each other in double direct shear (described in Section 2). Intermediate scale experiments lend confidence that the results can be up-scaled while at the same time precise measurements can be made of shear stress on the fault, slip displacement, ambient temperature, normal stress on the interfacial faults, sliding velocity and the hold time for which the ice has been static. This gives a level of resolution usually associated with small scale laboratory tests (e.g., Ohnaka and feng-Shen, 1999) [26] but not achievable in experiments in the Arctic Ocean due to the hostile environment (e.g., Scourfield et al., 2015) [2]. In Section 3, we present our results in terms of the spatial-temporal representation of slip in the rock and earthquake mechanics nucleation and propagation process. In Section 4 we discuss the results and unifying approaches across scales. In Section 5 we test the micro mechanical friction law of Hatton et al. (2009) [6] against our experimental data. We discuss the implications of our results and conclude with a suitable form for the friction law that could be applied at an Arctic Basin scale.

2 Experimental method

2.1 Test basin experiments

For our experiments, we used the Arctic Environmental Test Basin of the Hamburgische Schiffbau-Versuchsanstalt (HSVA), Hamburg (Fig. 1) (Sammonds et al., 2005) [28]. The basin is 30m long, 6m wide and 1.2m deep and filled with saline water, with salinity approximately 35 ppt; the same as ocean water. A motorized bridge spans the basin, on which is mounted a carriage for the operator. Air temperature can be regulated between -20°C to +20°C. To produce an ice sheet, saline water

from the basin is sprayed onto the water surface to produce an ice skim and then the temperature is lowered to grow the ice sheet. An ice sheet may be grown at an initial rate of up to 2 mm thickness per hour, but as the sheet thickens the growth rate slows considerably. Once the ice sheet has been grown to roughly the desired thickness the air temperature is then set to the desired test temperature. The effect of this is to produce a saline ice sheet, with roughly controllable thickness, of predominantly columnar- grained ice.

An ice sheet was grown at a nominal air temperature of -15°C to an average thickness of 168mm over several days. Over the 3-day course of our experiments the ice sheet continued to thicken slowly. The thickness was monitored by auguring in several places on the ice sheet, twice a day. The difference in ice sheet thickness across its expanse was 8mm. For day 1 and day 2 the average air temperature in the test basin was -7°C; the ice sheet thickened by 2mm on average. For day 3 the average air temperature was -11°C and the ice sheet thickened to 174mm on average. The time for the ice sheet to respond to a new set temperature was about 15h. Air temperature was monitored continuously at four locations in the ice basin chamber, 2m above the ice sheet, and water temperature at three locations along the length of the basin at different depths. The air temperature showed a gradient of about 2°C along the length of the ice sheet and about 0.5°C across its width, and was controlled to better than 1°C during a day. The water temperature showed remarkable consistency being -2.3°C at the shallower depth and -2.1°C at deeper depths with no measurable variations. The temperature profile of the ice sheet was monitored continuously by a thermistor string embedded in the ice sheet.

Temperature profiles of the ice sheet recorded during two friction tests on day 1 and day 2 are shown in figure 2. These roughly S-shape to linear profiles are both indicative of basal freezing and bottom accumulation conditions. Thin sections taken from a block cut from the ice sheet at the end of the experimental program are shown in figure 3, viewed under cross polarizing lenses. Two parallel sets of thick sections were cut perpendicular to the length of the test basin and one set of thick sections were cut parallel to its length. Three horizontal thick sections were cut at depths of 15 mm, 90 mm and 180mm in the plane of the ice sheet. Thin sections were made using standard techniques. A pair of representative vertical sections, cut through the thickness of the ice sheet, and two horizontal sections at 15 mm and 90 mm depth are shown. The sections show that the ice sheet consists of a layer of fine grained granular ice at the top, but columnar grain growth is quickly established, with a columnar grain width of over 10mm on average (Fig 3a). Surface roughness of the sliding fault surfaces were measured. In figure 3b a surface topographic profile is shown. Casts were made of surfaces using a quick-curing, high-resolution rubber solution (Microset 101RF) and the surface profile measured using a Proscan optical profilometer. These data are presented in Hatton et al. (2009) [6] Supplementary Material. As discussed we believe that this surface topography is controlled primarily by the sliding process producing a fractal surface (Scott et al., 1994) [30]. We believe this provides evidence that sea ice floes in the Arctic Ocean, which have undergone a similar repeated-sliding process, will have similar topography.

2.3 Friction experiments

The configuration for our experiments was the double-direct shear friction test (or mode II fracture mechanics test), analogous to that used in small-scale rock mechanics experiments (e.g., Ohnaka and feng-Shen, 1999) [26]. As shown in figure 4, a central free-floating ice floe (B), measuring 1.2 m by 6.5 m was pushed between two floating ice floes (A and C) along parallel pre-cut faults. The central floe is pushed by pusher plate mounted on the motorized rail-mounted bridge which spans the width of the test basin (Fig. 1). The bridge can move at nominal speeds ranging from 210 μm/s to 7 mm/s. The load normal to the fault surfaces is applied by six air-activated actuators mounted as pairs on three floating wooden frames (Fig. 4). Normal load was set by the air pressure driving the

actuators. The ice floes were prepared for experiments by cutting the ice sheet using a pair of cutters mounted on the test basin bridge. In this way parallel faults could be ensured.

The instrumentation set-up is shown schematically in figure 4 and can be seen in figure 1. Frictional load (F) was measured by two 20kN load cells mounted between the pusher plate and the cantilever attaching it to the carriage of test basin bridge. Normal load (N) was measured by six 10kN load cells mounted in pairs on the pneumatic rams on the floating normal load frames. The slip displacements (D_j, $j \in \{1,2,3,...,8\}$) on the central floe relative to the outer floe were measured by four 1m long stroke potentiometer displacement transducers mounted along each of the interfacial faults. Normal displacements were measured by a series of six 20mm stroke potentiometer displacement transducers, spaced at 1 m intervals, mounted across the fault. Local shear stresses (τ_i, $i \in \{1, 2, 3, \ldots, 8\}$) were measured by 16 stress sensors frozen into the ice floe and mounted in pairs as two limbs of rosettes. These stress sensors were 100 mm diameter mercury pressure pads described by Duckworth and Western (1989) [29]. Eight acoustic transducers were frozen onto the ice to monitor and locate acoustic emissions.

We undertook a series of lubricated double-direct shear friction tests on saline ice floes over a range of nominal speeds from 210μm/s to 7mm/s, a series of hold times, two set air temperatures, -7°C and -11°C, and a range of normal loads from 0 to 100kN. When the frictional load (F) was applied by the test basin bridge to the central ice floe either frictional sliding took place or the floe would not move. Frictional sliding took a stick-slip form, where shear load is applied the central ice floe remains stationary for some time, while clearly-visible flexural strain built up in the pusher plate, before the central ice floe suddenly and briefly moved forward, allowing the flexural strain in the pusher plate to relax; this cycle was then repeated, as long as the bridge kept driving forward. An example of results from an experiment is shown in figure 5. Here shear stress in the central ice floe is plotted against the slip displacement of the floe for several stick-slip cycles, chosen arbitrarily from a complete run. (The origin is arbitrary.) In this experiment the frictional force was applied at a nominal speed of 2.1mm/s. The nominal air temperature was -7°C; the ice floe temperature profile measured during this test is shown in figure 2 (the colder of the two temperature profiles). The typical normal load was 75kN, however no positive side load was applied by the actuators in this test.

2.3 Note on calibration

All force and stress measuring instruments were calibrated, prior to installation in the test basin by compressing them in series with the same load cell, of known sensitivity, offset and cross-sectional area. Similarly, all displacement-measuring instruments were calibrated against a steel rule. Visual inspection of plots of the output voltage against displacement, load or pressure of the instruments, as appropriate, confirmed their linearity, and least squares fitting was used to determine their sensitivities and offsets.

The freezing of the mercury stress sensors into the ice sheet and the bolting of the load cells to the pusher plate and to the normal load frames, were all capable of applying some force to the instruments and introducing extra offsets; in the first of these cases, the timescale-dependent and temperature- dependent mechanical properties of ice meant that the offset could vary with time. For the pusher plate load cells, this offset could be determined, by taking the arithmetic mean of measurements of force F, during an experiment (no. 20040122-1) in which the pusher plate was not brought into contact with the ice, and F was therefore known to be zero. For the normal load cells, we were able to use the knowledge that we never applied a tensile (i.e. negative) normal load N, to

identify a sudden drop with decreasing N in the frequency of occurrence of measurements, with zero normal load. For the shear-stress sensors, we identified those records where the ice was not being pushed (operationally defined as $|F| < 410N$) and was not moving (operationally defined as $|\dot{D}_j| < 330\mu m/s$) at times when the 9 shear stress τ_i was zero (the (i,j) pairs being those listed in figure 4). We then used the least-squares method to fit a polynomial function of time to the apparent shear stress in these records, and took this function to be the offset. The order of polynomial to fit was chosen by undertaking, separately for each shear stress transducer, a series of significance tests for the departure from zero of each successive polynomial coefficient. The significance tests were based on the decomposition of the marginal likelihood (typical goodness of fit) of a model (MacKay, 1992) [31], into a best-fit likelihood factor and an "Occam factor" which encodes how finely the model has tuned itself to the data. The highest-order polynomial chosen by the significance tests was a cubic (for transducer pair i = 6). In all cases, the results presented below have had the inferred offsets removed, by subtracting them from the apparent measurements.

3 Results: Spatio-temporal properties of slip events

In figure 6a we show the spatial and temporal changes in shear stress during a single stick-slip event. The nominal air temperature was -7°C; the ice floe temperature profile measured during this test is shown in figure 2 (the warmer of the two temperature profiles). Fig. 6b is a two-dimensional shear stress-time slice through the 3D plot. Initial mean normal load was 57kN. The shear stress, τ_i, in the central ice floe is plotted as a series of shear stress sensor positions $i \in \{1, 2, 3, \ldots, 7\}$ along the fault against time. (The stress sensor at position 8 did not yield data.) Data were collected at 5000 samples per second and the full sampling frequency is used in the plot. This diagram shows how high local shear stresses were initially induced at the pusher plate end of the ice floe and then propagated down the fault. The record at the first stress sensor position (i = 1) shows a gradually increasing shear stress with time, a peak stress, stress drop accompanying slip and then a return to a residual value. The strain pulse propagates in both space and time. There is a nucleation zone for slip covering the first two sensor positions ($i \in \{1, 2\}$), where the strain pulse is traveling slowly (at a minimum of 5.4 m/ s), followed by a propagation phase recorded at the sensor positions located along the fault (increasing distance x). The shear stress becomes impulsive (i.e. the wave-packet tends to a constant, narrow shape, which could also be described as a soliton) traveling along the fault at speeds in excess of 56 m/s (the highest we can measure). The speeds in the propagation phase are at least an order of magnitude higher than in the nucleation phase and we suspect will approach the Rayleigh wave speed in ice of about 1.7km/s (Stamoulis and Dyer, 2000) [32]. This cycle of stick-slip events is then repeated (not shown) as the floes continue to be pushed past each other. Our preliminary analysis of the locations of acoustic emissions indicates that all cracking associated with frictional sliding was constrained to the faults. No cracking was observed perpendicular to the faults.

In figure 6c we use a schematic map to illustrate this behaviour where we have plotted the time to the stress drop against position on the ice floe. Figure 6 is a demonstration of nucleation zone in the frictional slip of ice. Shear stresses monitored along the length of the fault surface show how non-uniformly local shear stresses are induced and accumulated along the fault during increase of the shear load and how gradually the fault strength degrades in a localized zone prior to sliding. After the initiation phase, where the shear stress is increasing slowly, there is a propagation phase where the shear stress increases rapidly with time and distance down the fault. The slipping region behaves like a wave-packet, propagating away from the nucleation zone.

In figure 7 we show five pairs of variables from among the local shear stress, the slip displacement, the velocity and the acceleration of the central ice floe, recorded at one location, during a single stick-slip cycle. The style of presenting data from a single stick-slip cycle is modelled on that of Ohnaka et al. (1987) [33]. For the variation of local shear stress with slip displacement (Fig. 7, top left panel) we see that the shear stress rises to a peak at a small but non-zero amount of slip and then decreases to a residual shear stress with on-going slip displacement. The shear stress then starts to rise for the next stick-slip cycle. This is slip-weakening behaviour which has also been observed during stick-slip along pre-cut faults in rock (e.g., Ohnaka et al., 1987 [33]). The slip-weakening failure energy can, in principle, be obtained from the plot of shear stress versus slip displacement in an analogous manner to rock. In the top right panel of figure 7 we see that the peak stress is attained at non-zero slip velocity. The slip velocity and acceleration are also plotted in figure 7 against displacement. Both accelerating and decelerating phases are clearly seen.

4 Mechanics of Frictional Slip

This paper focuses on frictional slip propagation during stick slip behaviour. Steady-sliding is also an important frictional phenomenon which has been the usual subject for experimental research and modelling. But it seems likely that stick-slip behaviour plays a significant role in pressure-ridge building in the polar pack as well as controlling floe-floe sliding. Stick-slip in ice is a second-order frictional phenomenon likely to be controlled by a complex interplay of mechanisms and promoted by increasing normal stress and decreasing temperature. However little research has been done on the mechanics (Sammonds et al., 1998 [7]; Lishman et al. 2011 [25]; Lishman et al., 2013 [27]). In rock mechanics stick-slip is promoted by smooth surfaces indicating a strong dependence on the characteristic length of geometric irregularities on the fault surface (Sammonds and Ohnaka, 1998 [34]).

The strong similarity with stick-slip behaviour in rock allows us to model qualitatively the constitutive behaviour of ice floe friction in an analogous manner. When the tip of the slipping zone propagates, the shear stress reaches a peak value at the tip, behind which is a "breakdown zone" where the stress drops to the residual frictional sliding stress levels. The breakdown zone size, D_{BD}, is equal to the nucleation zone size at the point where the rupture starts to propagate dynamically (Fig. 6). This has been observed during the high-resolution rock friction experiments of Ohnaka and feng-Shen (1999) [26]. However in their experiments frictional slip nucleates at a zone of minimum shear strength. In our experiments, because of the relatively high homogeneity of saline ice compared to granite there is no strongly contrasting minimum shear strength. The area under the shear stress versus slip displacement curve (figure 7, top left panel) is the critical energy release or shear rupture energy, G_c, and D_c is the critical slip displacement required for the local shear stress to decrease from the breakdown strength, τ_{max}, to the residual sliding friction level, τ_{res}. (Using the terminology of Ohnaka et al., 1987, this is the breakdown stress drop breakdown, $\Delta\tau_{bd}$). A cycle of breakdown and re-strengthening process of stick-slip can be seen in terms of the shear stress and slip velocity (see the schematic figure 8, right-hand panel). In Phase I the shear stress increases to a maximum with increasing slip velocity ($d\tau/dt > 0$ and $d^2D/dt^2 > 0$). After the maximum shear stress the shear strength degrades rapidly with increasing acceleration to a level where the slip velocity has a maximum value. This is Phase II, the accelerating phase ($d\tau/dt < 0$ and $d^2D/dt^2 > 0$). In Phase III the slip movement is stabilized by a subsequent decelerating phase ($d\tau/dt < 0$ and $d^2D/dt^2 \leq 0$). In Phase IV, there is a re-strengthening ($d\tau/dt > 0$ and $d^2D/dt^2 < 0$). In Phase V the slip motion is stopped ($d\tau/dt > 0$ and $dD/dt = 0$) and time-dependent re-strengthening occurs.

The shear rupture energy, G_c, is related to the constitutive parameters $\Delta\tau_{bd}$ and D_c (Rice, 1980, [35]),

$$G_c = \int_0^{D_c} = 1/2\ \Gamma\ \Delta\tau_{bd}\, D_c \qquad (1)$$

where Γ is a dimensionless parameter dependent upon the specific form of the slip-dependent constitutive relation (Ohnaka and Yamashita, 1989 [36]). This is illustrated schematically in figure 8.

In earthquake mechanics it has been argued that while both the breakdown zone size, D_{bd}, and the critical slip displacement, D_c, increase in size with increasing scale, their ratio, Q_c , is independent of size-scale and for quasi-static slip weakening may be estimated by

$$Q_c \equiv \frac{D_c}{D_{breakdown}} = \frac{4(1-\nu)}{\pi}\frac{\Delta\tau_{breakdown}}{G} \approx \frac{\Delta\tau_{breakdown}}{G} \qquad (2)$$

where ν is Poisson's ratio and G is the shear modulus (Ohnaka et al., 1987 [33]; Rice, 1980 [35]). For dynamic rupture the breakdown shear stress has to be scaled by rupture velocity. In rock mechanics and earthquake mechanics Q_c is of the order of 10^{-3}.

5 Micromechanical Constitutive Law

5.1 Development of the Model

Friction laws based on micro-mechanics have a common conceptual framework: pressing two pieces of dry material together brings them into direct contact, over some fraction f of the total area A of the facing surfaces; this fraction is determined by the deformation of the asperities under the normal load N. A shear stress $T_{asperity}$ is then necessary to fail these direct contacts, giving

$$\tau = f\, T_{asperity} \qquad (3)$$

The diversity of friction laws arises because there are multiple possible mechanisms, both for the deformation of asperities under the normal load, which may be either ductile (Bowden and Tabor, 1967 [14]) or elastic (Archard, 1957 [24]), and for shear failure of the interface to be either ductile or brittle, or for a material typically near its melting point, such as ice, proceed (Bowden and Hughes, 1939 [37]; Oksanen and Keinonen, 1982 [16]) by the melting of material by the heat dissipated by friction and Couette flow of the consequent fluid layer. For materials in general the assumption of ductile deformation under normal load, along with the assumption of constant $T_{asperity}$, has been used to reproduce the classic (originally phenomenological) Amonton's law, with the coefficient of friction μ independent of normal stress. The assumption of elastic deformation under normal load, again with constant $T_{asperity}$, produces a friction law dependent on surface topography, with a power law dependence of friction on normal stress (Archard, 1957 [24]):

$$\tau \propto \sigma_n^{\,n} \qquad (4)$$

For the case where all the asperities are the same height, n = 2/3. Various workers have repeated the analysis for other surface topographies and produced a variety of power-law dependencies of τ on σn between 2/3 and 1 (see Hatton et al., 2009 [6]).

Slip weakening, where shear stress degrades rapidly with slip displacement before reaching a near-constant value are large displacements, can be modelled by a slip weakening factor, w_s ,

$$w_s = 1 + M \exp(-D^H / D_0) \qquad (5)$$

Physically this represents the effect of spatially non-uniform slip within an individual asperity contact (Yoshioka and Iwasa, 1996 [38]). D^H is the slip displacement (measured since sliding stopped in the previous stick-slip cycle). M and D_0 are *ad hoc* adjustable parameters. D_0 is a characteristic displacement for an asperity contact, representing the displacement required to make sliding velocity homogeneous across the asperity. Note this contrasts with the critical slip displacement which is the amount of displacement required for the shear stress to return to a residual level.

Lubricated (hydrodynamic) friction is where direct contact of the sliding surfaces is prevented by an intervening layer of fluid. The interfacial fluid may be generated through the frictional melting of ice at the interface [15, 16]. If the fluid layer is thick enough to behave in a laminar fashion then the shear stress is the ratio of the product of sliding velocity, dD/dt and fluid viscosity η to fluid layer thickness l,

$$\tau = \eta \dot{D} / l \qquad (6)$$

Hatton et al. (2009) [6] have revisited these standard approaches, taking account of the unusual mechanical properties of ice. These properties make several major differences to the resulting friction laws. 1) The stress in ductile deformation of sea ice is strain-rate-dependent, i.e., time-scale-dependent. For ductile deformation under normal load, the relevant time-scale is the length of time for which a typical contacting asperity has been in contact. This can be expressed in terms of the instantaneous sliding velocity, the instantaneous sliding acceleration, the typical length scale of an asperity along the sliding direction and introduces dependences on velocity and acceleration in the shear stress. For ductile shear failure of the interface, the strain rate is proportional to sliding velocity, again introducing velocity-dependence in the shear stress. 2) The stress-strain relationship in elastic deformation of ice is also time-scale dependent (Sinha, 1978 [39]); for elastic deformation under normal load, this again introduces velocity and acceleration dependences in the shear stress, albeit of a different form from those found for ductile deformation under normal load. 3) The brittle shear fracture stress of ice depends on the tensile longitudinal stress: where the shear failure of the interface is brittle, this perturbs the exponent in the power-law dependence of shear stress on normal stress (Rist and Murrell, 1994 [40).

Hatton et al. (2009) [6] proposed to unify the models for the response to normal load and the shear failure of the real contact, by a principle of maximum displacement for normal deformation, and of minimum stress for shear failure:

$$\tau = \max(f_{el}, f_{du}) \, \text{smallest}(T_{du}, T_{br}, T_{ml}). \qquad (7)$$

That is, they pick the largest value for real contact fraction (elastic f_{el} or ductile f_{du}) and the smallest value for shear strength (ductile T_{du}, brittle T_{br} or melting lubrication, T_{ml}).

This unified model contains four adjustable parameters, dimensionless melt-water expulsion displacement X, the dimensionless contact-breaking displacement Y, the dimensionless shear layer thickness Z and the typical normal asperity strain $\underline{\epsilon}$ (see figure 9). The predictions from this model have been presented by Hatton et al. (2009) [6]. (An alternative model has been proposed by Nielsen et al. (2008) [17] for a melting-lubrication model for rocks which could be applied to ice.)

Quantitatively, the melting-lubrication model predicts a shear strength:

$$T_{ml} = \frac{sgn\dot{D}}{\pi^{1/4} X^{1/2}} \left[\left[(\kappa c \rho_s)^{1/2} (T_m - T) / \left|\dot{D}\right|^{1/2} \right] + \left[(\kappa c \rho_s)(T_m - T)^2 / \left|\dot{D}\right| + 2\eta b \rho_l \left|\dot{D}\right| \right]^{1/2} \right] \quad (8)$$

where κ is the thermal conductivity of ice, c is the specific heat capacity of ice, ϱ_s is the density of ice, η is the viscosity of water, b is the specific latent heat of melting of ice, and ϱ_l is the density of the brine (Table 1). The melting temperature T_m is pressure-dependent (Hatton et al., 2009 [6]).

X is the typical distance the ice floe has to move between a fluid element being generated by melting, at the leading edge of an individual asperity contact and the fluid element being ejected at the trailing edge of the asperity contact (Fig. 9). X is a topographic property of our particular sample; its involvement in this model, but not its value, is established by Oksanen and Keinonen (1982) [16]. Therefore, we treat X as an adjustable parameter. Equation 8 has two particularly interesting properties. The first is that there is competition between terms in the interface failure stress $T_{asperity}$, involving the conduction of heat away from the fault, which decrease with increasing velocity, and terms involving melting and viscous dissipation, which increase with increasing velocity. This competition gives the graph of shear stress against velocity predicts a convex $\cup$ form, with a minimum shear stress at a finite velocity. The second is that the normal-load dependence of the pressure melting will convert the pure power-law normal-load dependence into multiple power-law regimes with different exponents which is inherited from the contact fraction f.

The asperity topography is shown schematically in Fig. 9. P_C represents the total number of asperity peaks per unit area on the surfaces and R_C represents the radius of curvature of a typical asperity peak for the smallest-scale of the three asperity populations, and P_B the total number of asperity peaks per unit area on the surfaces and R_B represents the radius of curvature of a typical asperity peak for the medium-scale of the three asperity populations, d_G represents the ice grain size and Y represents the length of a typical individual asperity contact. These parameters are topographic properties of our particular sample. Their involvement in this model are discussed by Hatton et al. (2009 [6]). We treat $P_B{R_B}^2$, $P_C{R_C}^2$, d_G, and Y as adjustable parameters within bounds.

Models of the contact fraction f are based on elastic or plastic deformation under the normal load of a variety of surface topographies. The theoretical model for a two-stage "fractal" distribution of peak heights, by which is meant a population of identical, hemispherical asperities, on whose surfaces is another population of smaller, identical hemispherical asperities, on whose surfaces in turn is a third population of still smaller identical asperities (Archard, 1957 [24]. In reality, it does not matter whether the asperities are configured in exactly this fashion: all that is important is that the frequency density distribution of peak heights is the same as if they were distributed this way. When we re-visit the Archard model, using the timescale-dependent Young's Modulus and temperature-dependent Poisson's ratio of ice, we find a real contact fraction:

where p, d_0 and β_0 are empirically-determined properties of delayed elastic strain in ice, Q is an activation energy for the delayed elastic strain, R is the molar gas constant and E_P is the prompt Young's Modulus of ice (Table 1). The Poisson's ratio, ν, depends (Sinha, 1989 [39] linearly on temperature.

$$f_{fractal} = \frac{3^{65/27}\pi^{46/27}\left(1-\upsilon^2\right)^{26/27} {P_B}^{1/9} {P_C}^{1/3} {R_B}^{2/9} {R_C}^{2/3} N^{26/27}}{13 \times 2^{92/27}(E_P A)} \cdot \frac{\left(1 + \frac{d_0}{d_G}\left(1 - exp\left(-exp\left(\left(-\frac{Q}{RT} - \beta_0\right)t^H\right)^P\right)\right)\right)^{26/27}}{13 \times 2^{92/27}(E_P A)^{26/26}}$$

(9)

The time for which a typical individual asperity contact has existed, t^H, is:

$$t^H = \frac{\dot{D} \pm \sqrt{\dot{D}^2 \pm 2Y\ddot{D}}}{\ddot{D}} \qquad (10)$$

Hatton et al. (2009) [6].

The contact fraction $f_{fractal}$, the shear strength T_{ml} and the slip-weakening factor w_s can be combined to produce a theoretical expression for the shear stress required for sliding:

$$\tau = f_{fractal}\, T_{ml}\, w_s \qquad (11)$$

The total number of adjustable parameters is7; our data-set contains something of the order of 108 points, so we expect it to be capable not only of supporting seven adjustable parameters, but also of estimating their values with precision.

5.2 Fitting experimental data to the micromechanical model

Our data set, from multiple stick-slip events from 22 experimental runs, is of the order of 100 million data points. This has been smoothed to about 3 million data points for computation efficiency (c.f., Ohnaka and feng-Shen, 1999 [26]). As discussed below we found using a maximum likelihood approach that a fractal distribution of asperities, undergoing elastic normal load deformation, and deforming in shear with melting lubricating the sliding surfaces produces the best fit with the experimental data.

From the point of view of testing a frictional constitutive law (i.e., an equation for shear stress in terms of other variables, which may include temperature, normal load, acceleration, velocity and displacement since the last time the ice stopped sliding) it is useful to plot shear stress against other variables while the other four variables are held constant. Figure 10 shows where the dependent variable, shear stress τ_i in the central floe, is plotted against: a) the slip displacement of the central ice floe, D_j^H, since the last time it stopped plotted on a log scale to show the behaviour at low slip; b) the velocity and e) the normal load N. In Fig. 10c the coefficient of friction, τ_i A/N, is plotted against normal load. The data are from all 22 experiments done over a range of normal stresses, temperatures, hold times and speeds, representing many hundred of individual stick slip events. In each plot, constant values of the four independent variables not displayed (i.e., four out of displacement, velocity, acceleration, normal load and temperature) are simulated by selecting for inclusion only those samples where the four variables were within specified narrow ranges. These narrow ranges were:

$410\ \mu m \le D_j^{(H)} < 670\ \mu m$ $\qquad$ $4.1563\ mm.s^{-1} \le D_j < 6.7563\ mm.s\text{-}^{1}$

$-32.5\ mm.s^{-2} \le D_j < 32.5\ mm.s^{-2}$ $\qquad$ $111.2\ kN \le N < 116.6\ kN$

$268.82\ K \le T < 269.01\ K.$

There is no plot of shear stress against temperature as the control ranges used for the extraneous variables are so tight that once displacement, velocity, acceleration and normal load are controlled, all the half-dozen or so measurements that remain are at the same temperature.

The data are somewhat noisy but that does not prevent lineations being visible in the plots or formal statistical testing of friction laws. The first lineation is in the shear stress against displacement graph (Fig.10a), where the shear stress rapidly decreases with increasing displacement, before reaching a near-constant value at large displacement. This militates in favour of the idea that displacement-independent friction laws are large-displacement, equilibrium limits. To model this we introduce the slip-weakening factor (Equation 5). In the shear stress against velocity plot (Fig. 10b) there is a convex lineation is convex with a minimum shear stress at finite velocity. Below we discuss theoretical models involving failure of the interface through frictional heating, surface melting, and hydrodynamic lubrication, and will show that these are, in principle, capable of reproducing such a minimum. In Fig. 10c of the coefficient of friction is plotted against normal load and (equivalently) the shear stress (Fig. 10d) against normal load. The shear stress appears to follow a straight line on these logarithmic axes, which indicates a power-law dependence but with an exponent close to 1. Theoretical models involving elastic deformation under the normal load produce power laws for the shear stress as a function of normal load with exponents ranging between 2/3 and 1, depending on the surface topography. At high normal loads (Fig. 10d) there is a change of gradient which results from pressure-melting effects in melting/hydrodynamic lubrication. There is no plot of shear stress against acceleration as there was no clear lineation.

The theoretical model that is favoured by our experimental data involves failure of the interface through frictional heating, surface melting and hydrodynamic lubrication (equation 8).

6 Discussion

6.1 Stick-slip behaviour and slip wave propagation

The stick-slip behaviour illustrated in Figures 6-8 is highly reminiscent of the nucleation and propagation of a wave-packet, the order parameter that fluctuates in the wave-packet being sliding velocity: in a "nucleation zone," within ~1.5m of the pusher plate, the shear stress on the fault builds, along with the flexural strain in the pusher plate. This shear stress resists the load from the pusher plate, keeping the ice stationary. It also shields the rest of the fault from the effects of the pusher plate, keeping the shear stress outside the nucleation zone low. The nucleation zone becomes a zone of greatest shear stress. Eventually this shear stress becomes so great that the fault can no longer sustain it and the ice in the nucleation zone begins sliding, allowing the flexural strain in the pusher plate to relax and thereby unloading the ice. As the nucleation zone slides, the section of fault at the boundary of the nucleation zone is subject to a rapidly increasing shear stress, because the ice behind it is moving forward, pushing on it, while the ice in front of it remains stationary (in other words, the time- derivative of shear stress is proportional to the spatial derivative of velocity). The slipping region (wave-packet) then propagates along the fault; when it reaches the end of the ice, the ice returns to rest, and the cycle begins again. In a sense, this wave-like behaviour is not surprising as the time-derivative of shear stress is proportional to the spatial derivative of velocity. Friction laws discussed earlier relate shear stress to velocity, creating a relationship between the spatial derivative of velocity and the time-derivative of velocity, i.e., a wave equation for the velocity.

There is evidence for this occurring in the central Arctic sea ice pack from the SIMI experiment of 1994. Stamoulis and Dyer (2000) [32] analyzed hydrophone records of seismic waves radiated by fractures to estimate fracture velocity. They measured velocities from less than 100 ms-1 to 1100 ms^{-1}: well below the Rayleigh wave velocity of 1700 ms^{-1}, which should bound the velocity of propagation of shear cracks in ice. These measurements are consisted with our proposal for nucleation and propagation phases for shear rupture in sea ice.

From Fig. 7 we can see that the breakdown zone size, $D_{breakdown}$, is approximately 1.5m long. Typical critical slip displacements, D_c , (Fig. 8) are about 3mm. Therefore the ratio, ε_c , is about 2 x 10^{-3}. This is roughly the ratio found in rock and earthquake mechanics (Ohnaka and Shen, 1999) [26] and seems to suggest that we could expect this ratio to be scale independent. From Fig. 8 the breakdown shear stress, $\Delta\tau_{breakdown}$, is approximately 40kPa. The shear modulus of saline ice, G, is about 2.9 GPa (Sanderson, 2011) [41]. So their ratio is about 10^{-5}. In our experiments we are propagating rupture at low normal stresses and low shear stresses. Ohnaka et al. (1987) [33] note that in rock mechanics εc ranges from 10^{-5} to 10^{-3}, depending on normal stress. So again this is within the expected range. The shear rupture energy, G_c (Equation 1), is approximately 13 kJm^{-2} for the test shown in Fig. 8. By comparison, small- scale stick-slip experiments in rock mechanics give shear rupture energies of about 1 Jm_{-2} and major earthquakes values of 10^6 to 10^8 Jm^{-2} (Ohnaka and feng-Shen, 1999) [26]. This illustrates the strong control the critical slip displacement has on shear rupture energy and opens up a fracture mechanics approach to modelling the arctic sea ice cover.

6.2 Constitutive law for sea ice friction

We employed a friction law that can be incorporated into geophysical-scale sea ice rheological models, when coupled with a fault population model (Hatton et al., 2009) [6]. Physically, this law represents a situation where the ice deforms elastically under normal load, has a fractal distribution of asperity heights and fails in shear by melting and hydrodynamic lubrication. Interestingly, in achieving this very good global fit, the parameter estimation algorithm has not placed the minimum of shear stress with respect to velocity in the location where our visual inspection of the data suggested that it may be, nor has it placed a change in exponent of the shear stress as a function of normal load, in the location where we tentatively identified a step-like feature in visual inspection, nor indeed has it chosen a characteristic displacement length scale D_0 as long as we might have estimated by visual inspection. In all three cases, it has found the overall magnitude of the shear stress to be a more important consideration in choosing parameters than the location of these second-order features.

It is also interesting that we find elastic deformation of asperities under normal stress to be the appropriate mechanism. Acoustic emissions measured during the sliding indicate brittle fracture of asperities is going on. There is also wear on the sliding surface. However these brittle fracture processes at the asperity scale are not as important as the elastic deformation of asperities in determining the overall magnitude of the shear stress. At a larger scale of the propagation of the slip displacement during sliding, shear rupture can of course be modelled by fracture mechanics (Ohnaka and feng-Shen, 1999) [26], as discussed above. It should be noted that for the plots of shear stress and the coefficient of friction (Fig. 10d), the intersection with the step-like constant normal load (above 100kN) occurs where we believe pressure melting becomes important.

Archard (1957) [24] proposed a fractal asperity distribution before the term fractal was coined. There are three radii of curvature involved in the topography: R_C (small asperities), R_B (medium asperities) and R_A (large asperities). However, only small asperities (R_C) and medium asperities (R_B) are involved in the friction law. Physically, increasing R_A brings more medium asperities on any one large asperity into contact, but also increases the total number of medium asperities on the large asperity, so that the fraction of the medium asperities that are in contact stays constant. In addition, increasing R_A increases the load on, and therefore the contact area, of medium asperities at any given distance from the large asperity centre. But increasing R_A also brings into contact

medium asperities further out from the large- asperity centre, so that the typical area contributed by a contacting medium asperity stays constant. Overall, the value of increasing R_A has no effect on the mechanics.

7. Conclusion

We have presented results from frictional sliding experiments on floating saline ice floes in the HSVA ice tank. These experiments broadly simulate conditions of temperature, strain rate and shear stress found in the high Arctic Ocean. We found that frictional slip is predominantly by quasi-cyclic stick-slip behaviour. A stick-slip cycle takes the form of repeated nucleation near the pusher plate and propagation along the fault of spatially and temporally localized wave-packets in the sliding-velocity field. The ice-ice friction law is characterized by slip-weakening, i.e., by a frictional shear stress that decreases with increasing sliding displacement for small positive sliding displacements, then reaches a near-constant value for larger sliding displacements. The constitutive law for lubricated friction of sea ice floes follows Archard's law rather than Amonton's law, with $\tau \propto \sigma_n^{\,n}$, with n = 26/27. The surface asperities deform elastically under normal load but the interface fails in shear through a process of frictional heating, localized surface melting and hydrodynamic lubrication.

We therefore propose, for inclusion in geophysical-scale sea ice models, the single-fault shear-stress friction law, fractal asperity height distribution, melting lubrication and slip weakening model:

$$\tau = f_{fractal}\, T_{ml}\, w_s$$

with the following values for the adjustable parameters of the law: X = 5.3 μm, Y = 44.1μm, $P_C R_C^{\,2} = 2.83 \times 10^{-13}$, $P_B R_B^{\,2} = 1.42 \times 10^{-3}$, d_G = 6.9mm, D_0 = 36.9μm and M = 0.125 .

Additional Information

Acknowledgments
We thank the Hamburg Ship Model Basin (HSVA), especially the ice tank crew, for the hospitality and technical support and Richard Rabe, Steve Boon, John Bowles, and Neil Hughes at UCL for engineering support. We thank Ben Lishman for helpful discussions. DLF and DCH acknowledge financial support made available from the Leverhulme Trust. DCH acknowledges financial support from Rio Tinto.

Funding Statement
This research was funded by the UK Natural Environment Research Council. Access to the Research Infrastructure ARCTECLAB was financially supported within the 5th Framework Programme by the Improving Human Potential Programme from the European Union through contract HPRI-CT-2001-00126.

Competing Interests
We have no competing interests.

Authors' Contributions
Sammonds conceived the experiments. Hatton analysed the data. Hatton, Sammonds and Feltham executed the experiments, interpreted the data and wrote the article.

References

1. Seymour-Pierce, A., Lishman, B. & Sammonds, P. 2016 Recrystallisation and damage of ice in winter sports, *this volume*.

2. Scourfield, S., Sammonds. P., Lishman, L. & and Marchenko, M. 2015 The effect of ice rubble on ice-ice sliding, In: Proc 23rd Int. Conf. Port & Ocean Engineering under Arctic Conditions June 14-18, 2015 Trondheim, Norway.

3. McCarthy, C., Savage, H., & Nettles. M. 2016 Temperature dependence of ice-on-rock friction at realistic glacier conditions, *this volume*.

4. Weiss, J. & Dansereau, V. 2016 Linking scales in sea ice mechanics, *this volume*.

5. Middleton, C.A., Grindrod, P.M. & Sammonds, P.R. 2016 The effect of rock particles and D2O replacement on the flow behaviour of ice, *this volume*.

6. Hatton, D.C, Sammonds, P.R. & Feltham, D.L. 2009 Ice internal friction: Standard theoretical perspectives on friction codified, adapted for the unusual rheology of ice, and unified. *Philos. Mag.*, **89**(31), 2771–2799. doi: 10.1080/14786430903113769.

7. Sammonds, P.R., Murrell, S.A.F. & Rist, M.A. 1998 Fracture of multiyear sea ice. *J. Geophys. Res.*, **103**(C10), 21795–21815.

8. Kwok. R. 2001 Deformation of the Arctic Ocean sea ice cover between November 1996 and April 1997: A qualitative survey. In Dempsey and Shen [18], pp. 315–322.

9. Marko, J.R. & Thomson, R.E. 1977 Rectilinear leads and internal motions in the ice pack of the western arctic ocean. *J. Geophys. Res.*, **82** (C6), 979–987.

10. Hopkins, M.A., Tuhkuri, J. & Lensu. M. 1999. Rafting and ridging of thin ice sheets. *J. Geophys. Res.*, **104** (C13), 13605–13613. doi: 10.1029/1999JC900031.

11. Tuhkuri J. & Lensu. M. 2002 Laboratory tests on ridging and rafting of ice sheets. J. *Geophys. Res.*, **107** (C9), 3125. doi: 10.1029/2001JC000848.

12. Sammonds, P.R. & Rist, M.A. 2001 Sea ice fracture and friction. In Dempsey and Shen [18], pp. 183–194.

13. Taylor, P.D., Feltham, D.L., Sammonds, P.R. & Hatton. D.C. 2006 Continuum sea ice rheology determined from subcontinuum mechanics. *J. Geophys. Res.*, **111** (C11), C11015–1–C11015–14. doi: 10.1029/2005JC002996.

14. Bowden, F.P. & Tabor, D. 1967 *Friction and Lubrication*. Metheun & Company, London.

15. Evans, D.C.B., Nye, J.F. & Cheeseman, K.J. 1976 The kinetic friction of ice. *Proc. R. Soc. Lond. A*, **347**, 493–512.

16. Oksanen, P. & Keinonen, J. 1982. The mechanism of friction of ice. *Wear*, **78**, 315–324.

17. Nielsen, S., Di Toro, G., Hirose, T. & Shimamoto, T. 2008. Frictional melt and seismic slip. *J. Geophys. Res.* **113**, B01308. doi:10.1029/2007JB005122.

18. Persson, B.N.J. 2015. Ice friction: Role of non-uniform frictional heating and ice premelting. *J. Chemical Physics* **143**, 224701.

19. Rist. M.A. 1997 High-stress ice fracture and friction. *J. Phys. Chem. B,* **101**(32); 6263–6266. doi: 10.1021/jp963175x.

20. Barnes, P., Tabor, D. & Walker. J.C.F. 1971 The friction and creep of polycrystalline ice. *Proc. R. Soc. Lond. A*, **324** (1557), 127–155.

21. Kennedy, F.E., Schulson, E.M. & Jones, D.E. 2000 The friction of ice on ice at low sliding velocities. *Philos. Mag. A,* **80**(5), 1093–1110. doi: 10.1080/01418610008212103.

22. Maeno, N.M., Arakawa, A., Yasutome, A. & Kanazawa, S. 2003 Ice-ice friction measurements, and water lubrication and adhesion-shear mechanisms. *Can. J. Phys.*, **81**, 241–249.

23. Schulson, E. M. & Fortt, A.L. 2012 Friction of ice on ice, *J. Geophys. Res.*, **117**, B12204, doi: 10.1029/2012JB009219.

24. Archard. J.F. 1957 Elastic deformation and the laws of friction. *Proc. R. Soc. Lond. A*, **243**(1233), 190–205.

25. Lishman, B., Sammonds, P.R. & Feltham, D.L. 2011 A rate and state friction law for saline ice. *J. Geophys. Res.*, **116** (C05), C05011–1–C05011–13. doi: 10.1029/2010JC006334.

26. Ohnaka, M. & feng-Shen, L. 1999 Scaling of the shear rupture process from nucleation to dynamic propagation: Implications of geometric irregularity of the rupturing surfaces. *J. Geophys. Res.*, **104** (B1), 817–844.

27. Lishman, B., Sammonds, P.R. & Feltham, D.L. 2013 Critical slip and time dependence in sea ice friction. *Cold Reg. Sci. Tech.*, **90-91**, 9–13. doi: 10.1016/j.coldregions.2013.03.004.

28. Sammonds, P.R., Hatton, D.C., Feltham, D.L. & Taylor. P.D. 2005 Experimental study of sliding friction and stick-slip on faults in floating ice sheets. In Proc. 18th Int. Conf. Port and Ocean Engineering Under Arctic Conditions, vol. 1, pp. 303–312, Potsdam, New York, June 29 2005. Clarkson University, Clarkson University.

29. Duckworth, R. & Westerman, P.H. 1989 Stress and strain instruments developed for field measurements of ice. *IEEE J. Ocean. Eng.*, **14** (2), 159–165. doi: 10.1109/48.16829.

30. Scott, D.R., C. J. Marone, C.J. & C. G. Sammis, C.G. 1994 The apparent friction of granular fault gouge in sheared layers, *J. Geophys. Res.* 99 7231.

31. MacKay, D.J.C. 1992. Bayesian interpolation. *Neural Comput.*, **4**(3), 415–447. doi: 10.1162/neco.1992.4.3.415.

32. Stamoulis, C. & Dyer. T. 2000 Acoustically derived ice-fracture velocity in central Arctic pack ice. *J. Acoust. Soc. Am.*, **108,** 96–104.

33. Ohnaka, M., Kuwahara, Y. & Yamamoto, K. 1987 Constitutive relations between dynamic physical parameters near a tip of the propagating slip zone during stick-slip shear failure. *Tectonophysics*, **144,** 109–125.

34. Sammonds, P. R. & Ohnaka, M. 1998.Evolution of microseismicity during frictional sliding, *Geophys. Res. Letts.*, **25**, 699-702.

35. Rice. J.R. 1980 The mechanics of earthquake rupture. In Dziewonski A.M. & Boschi, E. eds., *Physics of the Earth's Interior*, pp. 555–649. North-Holland, New York.

36. Ohnaka, M. & Yamashita, T. 1989 A cohesive zone model for dynamic shear faulting based on experimentally inferred constitutive relation and strong motion source parameters. *J. Geophys. Res.*, **94** (B4), 4089–4104.

37. Bowden, F. P. & Hughes, T.P. 1939 The mechanism of sliding on ice and snow, *Proc. Roy. Soc. Lond. A Mat.*, **172**(949), 280–298.

38. Yoshioka, N. & Iwasa, K. 1996 The characteristic displacement in rate and state- dependent friction from a micromechanical point of view, *PAGEOPH*, **147**, 433-453.

39. Sinha, N.K. 1978 Rheology of columnar-grained ice, *Exp. Mech.*, pp. 464–470.

40. Rist, M.A. & S.A.F. Murrell 1994 Ice triaxial deformation and failure, *J. Glaciol.*, **40**(135), 305–318.

41. Sanderson, T.J.O. 2011 *Ice Mechanics and Risks to Offshore Structures*, Springer, Dordrecht, Netherlands pp. 270.

Figure and table caption

Table 1
Table of variable and parameters used in the micromechanical models (see Hatton et al, (2009) [6]).

Figure 1
Photograph of the HSVA Arctic Environmental Test Basin showing our experimental set-up for a lubricated double-direct-shear test on floating saline ice floes. The bridge across the basin is used to push a central block of ice between two side blocks which apply a normal load, provided by side pusher panels (bottom left). The basin is 30 m long by 6 m wide.

Figure 2
Temperature profiles of the ice sheet are shown for two experiments discussed in the text done on Day 1 and Day 2 of the test program. The nominal air temperatures were –7°C and –6°C respectively.

Figure 3
a) Pair of vertical thin sections taken through the thickness of the ice sheet and two horizontal thin sections taken at 15 mm depth (top) and 90 mm depth in the plane of the ice sheet, viewed under crossed polarizing lenses. The grid size is 10 mm × 10 mm. (See Hatton et al. (2009, Fig. 9 and supplementary online material B [6]). b) Profile of a replica surface taken from the frictional sliding surface. The direction of sliding is x and z is the vertical direction in the ice sheet. The area of the surface sampled is 10mm by 10mm.

Figure 4
Schematic diagram of the double-direct shear test in the HSVA environmental test basin. R1 to R8 denote the positions of 8 pairs of stress sensors mounted as two limbs of rosettes which measured local shear stresses. 6 transverse displacement transducers mounted at 1m intervals measured local normal displacement. D1 to D8 denote the position of 8 longitudinal displacement transducers, mounted to measure slip displacement. 8 acoustic transducers (not shown) recorded acoustic emissions.

Figure 5
The shear stress τ_4 in the central ice floe, during a single stick-slip event in experiment no. 20040121-4, is plotted, as points, against the displacement D_2; the subscripts “4” and “2” index the positions along the fault where the shear stress sensor and displacement were measured; these are roughly equivalent positions (see Fig 4). Data were collected at 5000 samples per second, and the full sampling frequency is used in this plot. $D_{(start-0)}$ is an arbitrary origin for displacement.

Figure 6
a. The shear stress τ_i in the central ice floe, during a single stick-slip event in experiment number 20040122-8, is plotted, as points, against the position x where the shear stress sensor was positioned and the time t; the subscript “i” indexes the position x. Data were collected at 5000 samples per second, and the full sampling frequency is used in this plot.
b. Schematic map of the processes taking place on the fault, as a function of position and time.

Figure 7

Five pairs of variables, from among the shear stress τ_4 in the central ice sheet, the displacement D_2 of the central ice sheet, the velocity $\dot{D}_2$ of the central ice sheet, and the acceleration 2 of the central ice sheet, during a single stick-slip event in experiment 20040121-4, are plotted, as points; the subscripts "4" and "2" index the positions along the fault where the shear stress sensor and displacement were measured; these are roughly equivalent positions (see figure 4). $D_{2(start-1)}$ is an arbitrary origin for displacement.
Top left: shear stress is plotted against displacement. Top right: shear stress is plotted against velocity. Middle left: velocity is plotted against displacement. Middle right: acceleration is plotted against displacement.

Figure 8
Schematic diagram (from figure 7). The behaviour shows an initial Phase I where peak shear stress is attained, an accelerating Phase II, a decelerating Phase III, a re-strengthening Phase IV, and in Phase V a time dependent strengthening. Bottom left: shear stress is plotted against acceleration.

Figure 9
Lubricated sliding asperity contact model. Two levels of asperities are shown (medium and smaller size, with radii of curvature, R_B and R_C respectively). Melt is generated at the contact and expelled. X is the distance the ice floe has to slide between a fluid element being generated by melting at the leading edge of an individual asperity contact and being expelled at the trailing edge. D_0 is a characteristic displacement representing the slip required for complete replacement of the real asperity contact area. Y is the contact destruction length representing the typical individual asperity contact during sliding.

Figure 10
The dependent variable, shear stress τ_i, in the central ice, during all the HSVA Hamburg experiments, is plotted, as points, against one at a time of the four independent variables, the velocity $\dot{D}_j$ of the central ice sheet, the acceleration $\dot{D}_j$ of the central ice sheet, the normal load N on the fault, and the temperature T of the ice, calculated as an arithmetic mean of the temperatures at the five depths, in the ice, where temperature was measured. Top left a: shear stress is plotted against displacement. Top right b: shear stress is plotted against velocity. Bottom left c: coefficient of friction is plotted against normal load. Bottom right d: shear stress is plotted against normal load.

Table 2

Measured variables			
A	Contact area		
N	Normal load		
σ_n	Normal stress		
τ	Shear stress		
D	Slip displacement		
$\dot{D}$	Slip velocity		
$\ddot{D}$	Slip acceleration		
D^H	Slip displacement since end of previous cycle		
T	Temperature		
d_G	Average grain size		
Calculated variables			
f	Asperity contact fraction		
$f_{fractal}$	Fractal asperity contact fraction		
T	Shear strength of an asperity		
T_{ml}	Shear strength of an asperity (melting-lubrication model)		
τ	Shear stress		
t^H	Asperity contact time		
w_s	Slip weakening parameter		
Adjustable parameters			
D_0	Characteristic displacement for sliding to become homogeneous across the asperity		
M	Slip weakening parameter		
X	Fluid loss length scale		
Fixed parameters: Universal thermodynamic and mechanical parameters			
C_{CC1}	Clausius-Clapeyron coefficient 1	84.3 nK Pa^{-1}	*Bowden and Hughes* [1939]
C_{CC2}	Clausius-Clapeyron coefficient 2	56.3 nK Pa^{-1}	*Chaplin* [2006]
E_P	Prompt Young's Modulus of ice	9.3 GPa	*Sinha* [1978]
Q	Activation energy for delayed elastic strain	65.7 kJ mol^{-1}	*Sinha* [1978], Sandesron [1988], *Sammonds et al.* [1998]
R	Molar gas constant	8.314472 J mol^{-1} K^{-1}	*Petley* [1995]
T_{m0}	Pressure free melting temperature of ice in 3.5 wt% *NaCl* brine	271.53 K	*Hall et al.* [1988]
b	Specific latent heat of melting ice	333 kJ kg^{-1}	*McGlashan* [1995a]
c	Specific heat capacity of ice	2097 J kg^{-1} K^{-1}	*Richardson* [1995]
d_0	Critical grain size for delayed elastic strain parameter	9 mm	*Sanderson* [1988]
p	Delayed elastic strain parameter	0.34	*Sinha* [1978]
β_0	Delayed elastic strain parameter	-22.339	*Sinha* [1978]
η	Viscosity of water	1.792 mPa s	*Watson* [1995]
κ	Thermal conductivity of ice	2.3 W m^{-1} K^{-1}	*Morrell* [1995]

Figure 1

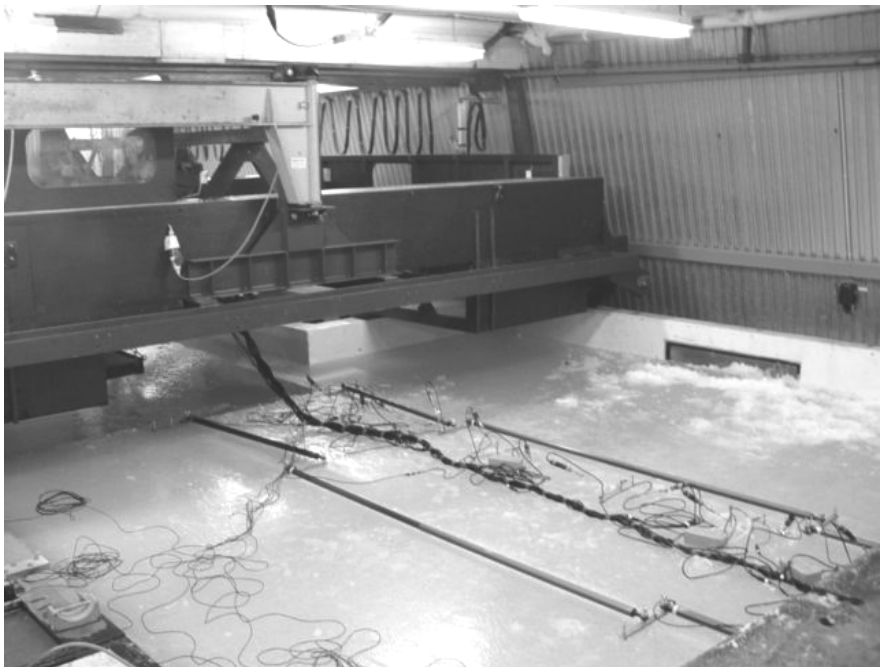

Figure 2

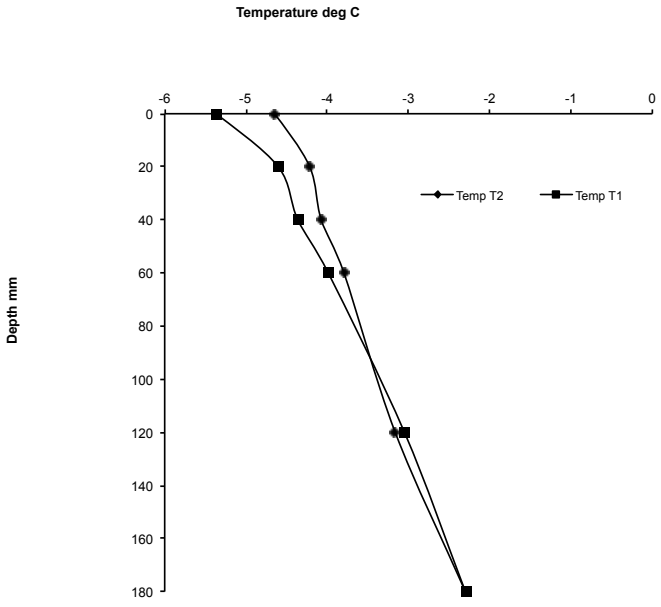

Figure 3

a)

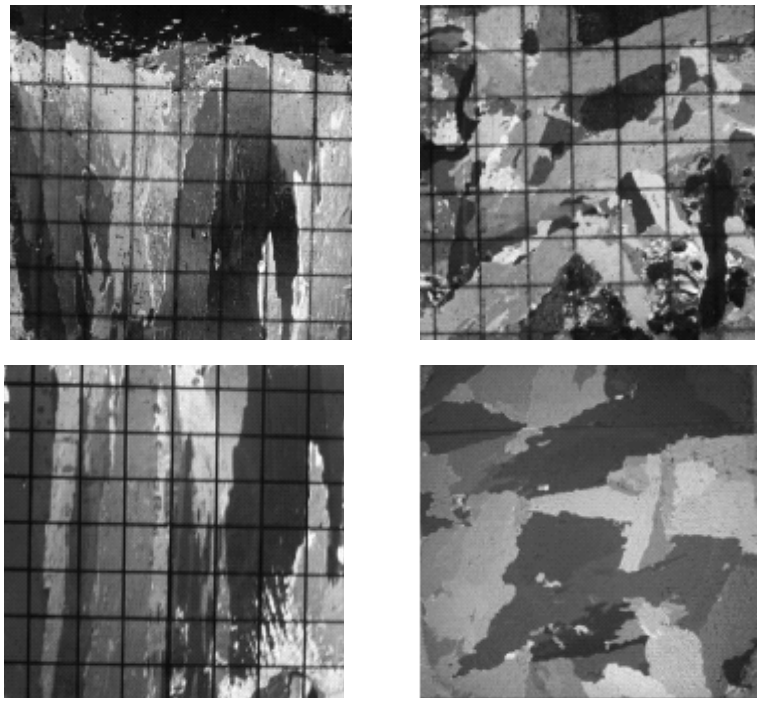

Vertical sections Horizontal sections

b)

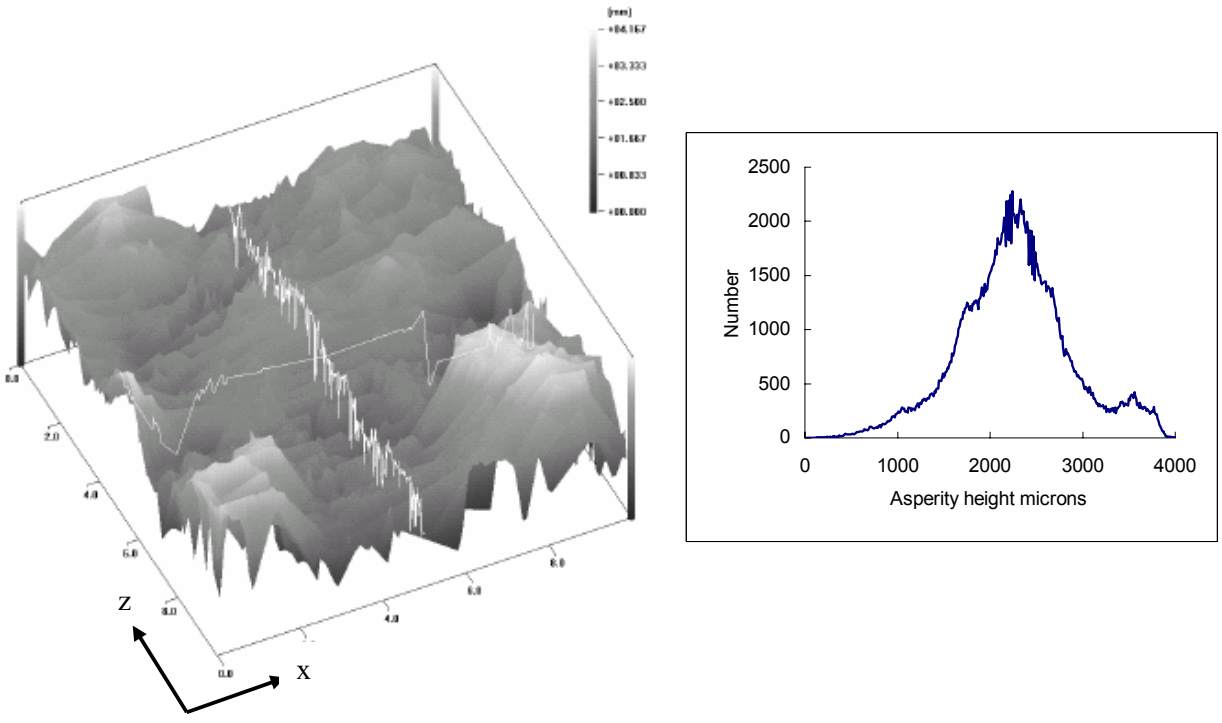

Figure 4

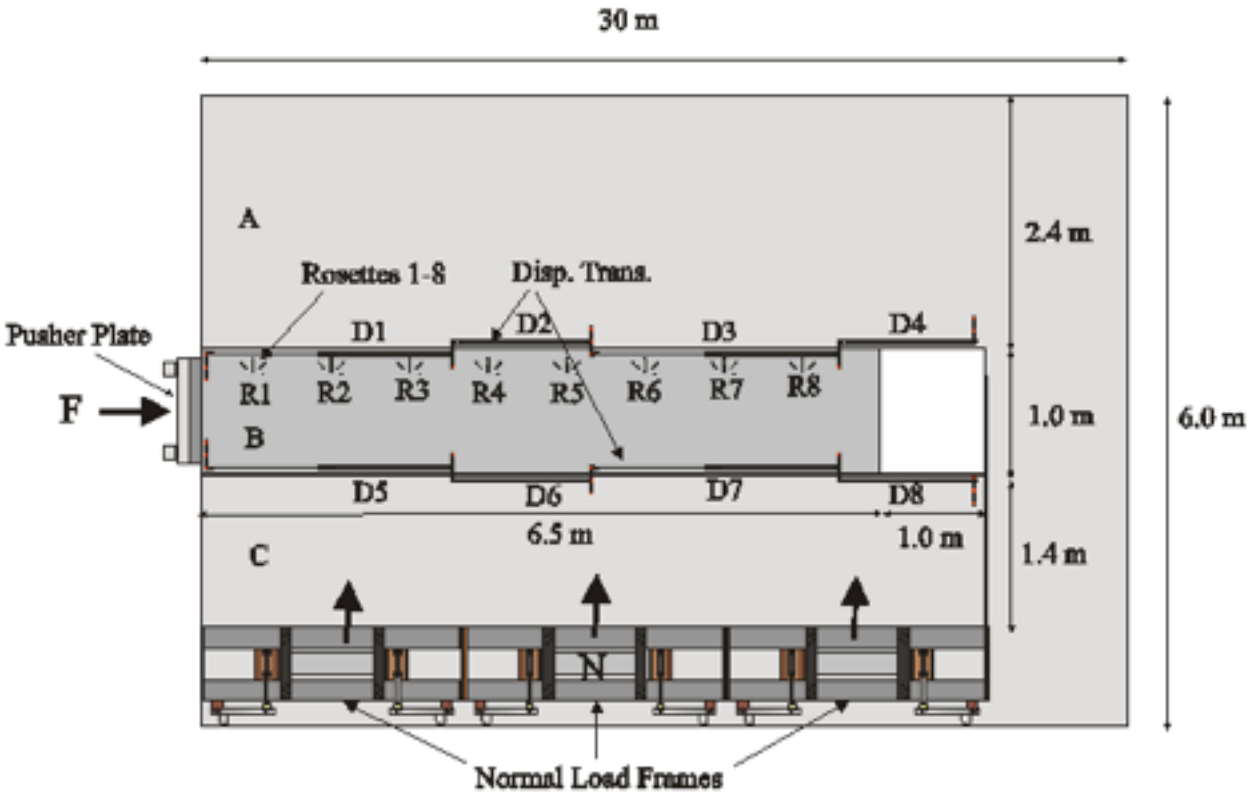

Figure 5

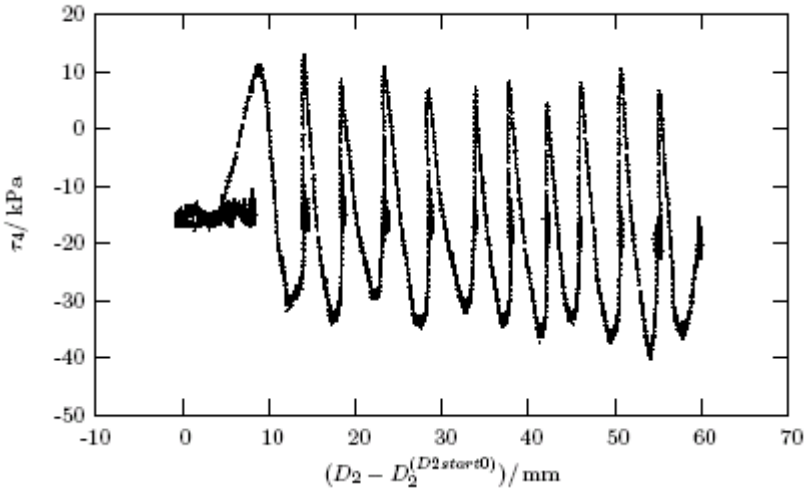

Figure 6

a)

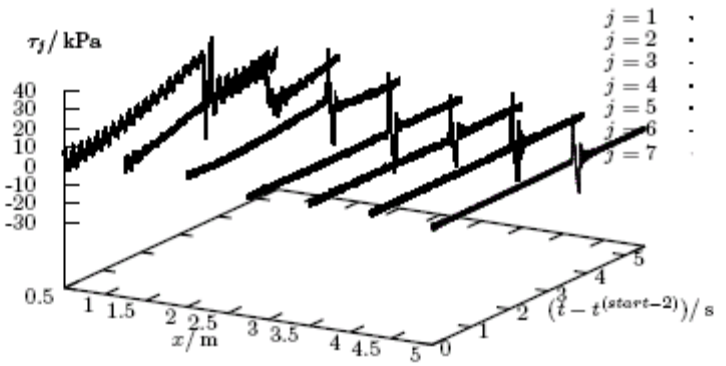
τ_j/ kPa
40
30
20
10
0
-10
-20
-30
0.5
1
1.5
2
2.5
3
3.5
4
4.5
5
x/ m
0
1
2
3
4
5
$(t - t^{(start-2)})$/ s
$j = 1$
$j = 2$
$j = 3$
$j = 4$
$j = 5$
$j = 6$
$j = 7$

b)

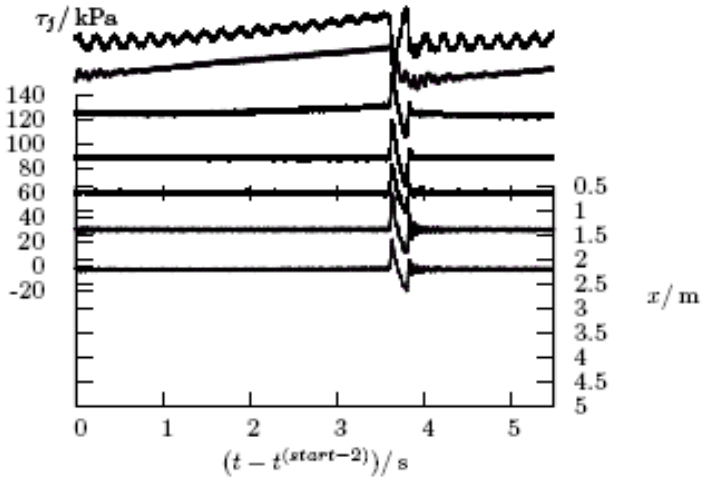
τ_j/ kPa
140
120
100
80
60
40
20
0
-20
0.5
1
1.5
2
2.5
3
3.5
4
4.5
5
x/ m
0
1
2
3
4
5
$(t - t^{(start-2)})$/ s

c)

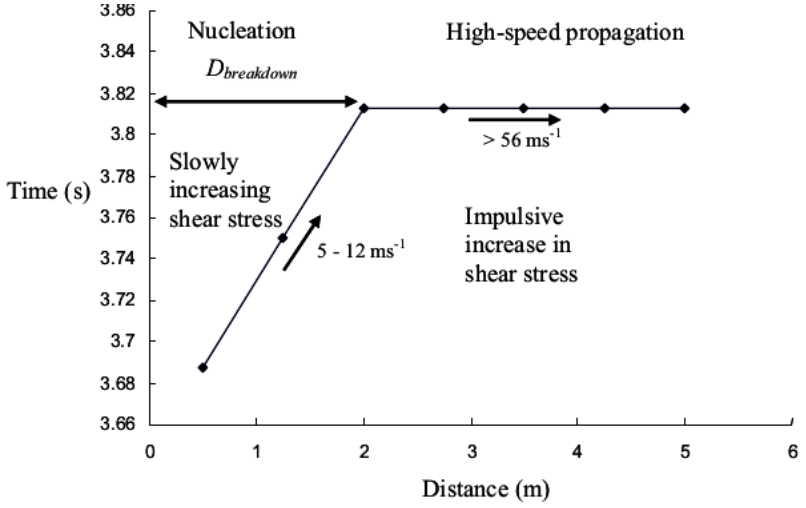
Nucleation
$D_{breakdown}$
High-speed propagation
> 56 ms^{-1}
Slowly
increasing
shear stress
5 - 12 ms^{-1}
Impulsive
increase in
shear stress
Time (s)
3.86
3.84
3.82
3.8
3.78
3.76
3.74
3.72
3.7
3.68
3.66
0
1
2
3
4
5
6
Distance (m)

Figure 7

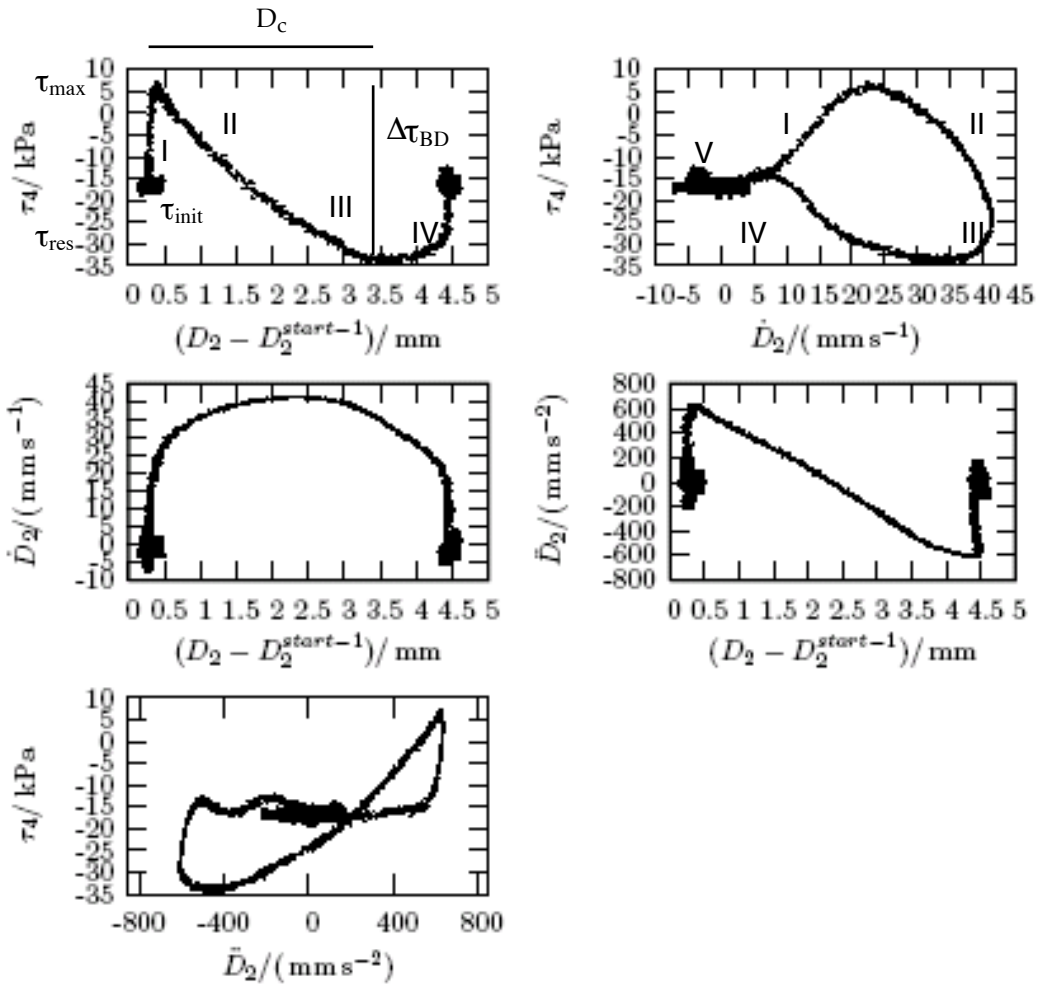
D_c
τ_max
τ_init
τ_res
Δτ_BD
I
II
III
IV
V
τ_4 / kPa
(D_2 − D_2^{start−1}) / mm
Ḋ_2 / (mm s^{−1})
D̈_2 / (mm s^{−2})

Figure 8

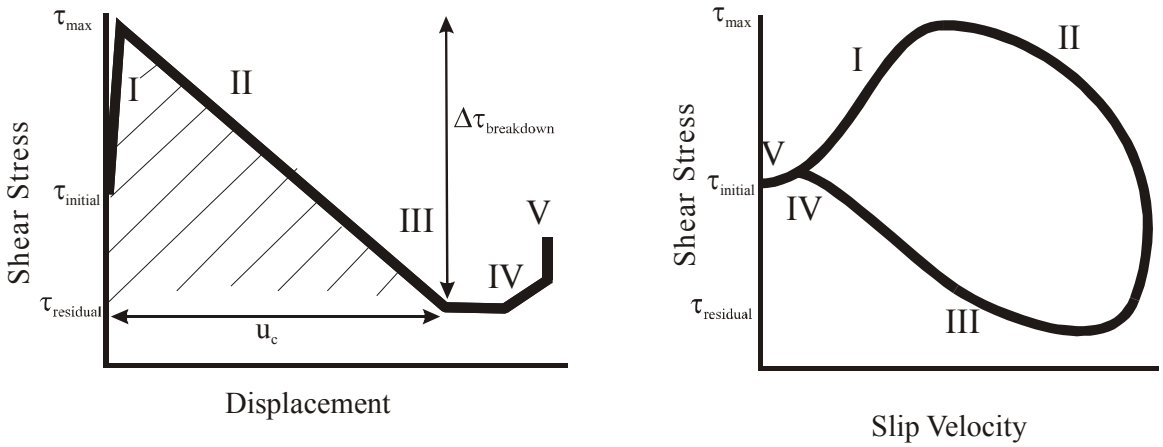
τmax
τinitial
τresidual
Shear Stress
I
II
III
IV
V
Δτbreakdown
uc
Displacement
τmax
τinitial
τresidual
Shear Stress
I
II
III
IV
V
Slip Velocity

Figure 9

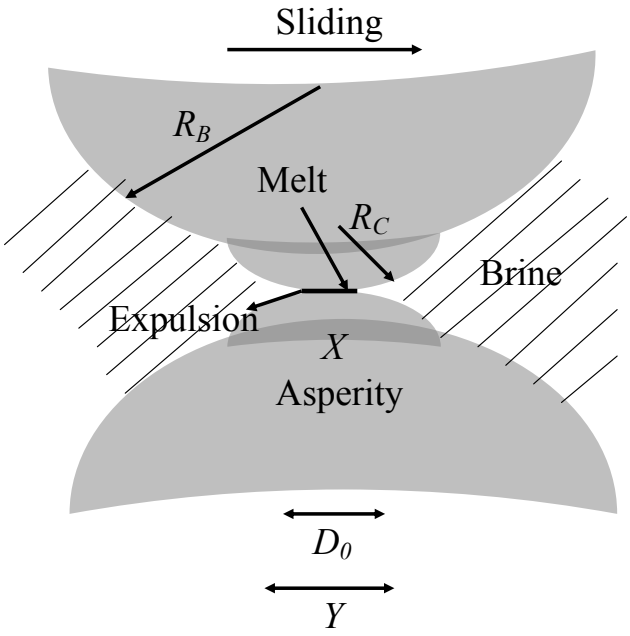

Figure 10